Multistage turbomachinery design using the discrete adjoint method within the open-source software su2

Vitale, S.; Pini, M.; Colonna, P.

Important note
To cite this publication, please use the final published version (if applicable).
Please check the document version above.

Multistage Turbomachinery Design Using the Discrete Adjoint Method Within the Open-Source Software SU2

S. Vitale,* M. Pini,† and P. Colonna‡
*Propulsion and Power, Aerospace Engineering, Delft University of Technology, 2629 HS Delft,
The Netherlands*

This paper documents a fully turbulent discrete adjoint method for three-dimensional multistage turbomachinery design. The method is based on a duality preserving algorithm and is implemented in the open-source computational fluid dynamics tool SU2. The SU2 Reynolds-averaged Navier–Stokes solver is first extended to treat three-dimensional steady turbomachinery flow using a conservative formulation of the mixing-plane coupled to nonreflective boundary conditions. The numerical features of the flow solver are automatically inherited by the discrete adjoint solver, ensuring the same convergence rate of the primal solver. The flow solver is then validated against experimental data available for three turbine configurations, namely, a one-and-half axial turbine stage, a transonic radial turbine coupled to a downstream diffuser, and a supersonic mini–organic Rankine cycle radial turbine operating with a fluid made by a heavy molecule. Finally the adjoint-based optimization framework is applied to the concurrent shape optimization of three rows of the axial turbine, demonstrating the advantages deriving from adopting multirow automated design methods in the context of turbomachinery design.

I. Introduction

THE use of computational fluid dynamics (CFD) has become irreplaceable within the turbomachinery design process. CFD provides the aerodynamicist with information that, in the past, had to be obtained with limited, greatly more expensive, and time-consuming wind tunnel experiments. Thus, the use of CFD has resulted in a substantial performance enhancement of turbines and compressors. However, such enhancements have become nowadays increasingly difficult to achieve. To improve the efficiency of just a fraction of a percentage point, the designer has to take into account such a vast number of aspects that the problem can be solved only by coupling high-fidelity CFD simulations with numerical optimization techniques.

The simultaneous optimization of multiple blade rows allows to achieve better performance if compared with the solution that would be obtained by optimizing each row separately. Although gradient-free optimization methods may still be a viable option for three-dimensional (3D) single-blade-row fluid dynamic design [1,2], adjoint methods are the only practical solution for multistage design because of the comparatively larger number of design variables [3].

The adjoint method was first applied to compressible fluid dynamic design problems by Jameson in 1988 [4], and since then it has been extensively applied to external flow problems [5–8]. However, due to the additional complexity of deriving the adjoint equations for internal flow problems, in particular for what concerns the linearization of the inflow and outflow boundary conditions, the application of adjoint-based optimization to turbomachinery design is less widespread and scarcely documented in the literature [3]. Only in recent years a research effort has been made to extend the adjoint method for turbomachinery applications. Some works have documented adjoint methods for single-blade optimization [9–14] and much fewer for multistage optimal designs [15–18]. In this case, the linearization of the mixing-plane interface is an additional challenge. Furthermore, nearly all the studies were restricted to the use of the constant

eddy viscosity (CEV) approximation [19] to avoid dealing with the differentiation of the turbulent transport equations.

The open-source CFD platform SU2 [20] has recently gained recognition because of the implementation of a flexible, accurate, and efficient discrete adjoint (DA) solver [21]. The DA solver is automatically derived by means of advanced algorithmic differentiation techniques [22]. Various applications of this new design framework have been presented. Albring et al. [21] described an application of the SU2 DA solver to external aerodynamic problems; Becket et al. [23] showed the possibility of employing it for the design of wings taking into account aeroacoustic constraints; Sanchez et al. [24] used it for the solution of aeroelasticity problems in aeronautics; Vitale et al. [25] employed the DA to show how the aerodynamic performance of single-blade organic Rankine cycle (ORC) turbine cascades can be improved, but limited to two-dimensional (2D) test cases; finally, Rubino et al. [26] extended the DA solver in order to perform the unsteady optimization of 2D cascades using the harmonic balance method. However, although these last two efforts demonstrate the feasibility of deriving an accurate and efficient fully turbulent adjoint for turbomachinery applications within the SU2 design framework, yet the solution of industrially relevant problems requires the extension of those approaches to handle 3D multistage turbomachinery.

Therefore, the work described here documents the extension and validation of the DA solver of SU2 to 3D fully turbulent multistage turbomachinery applications. To reach this objective, the SU2 Reynolds-averaged Navier–Stokes (RANS) solver was first enriched with the implementation of a conservative and nonreflecting mixing-plane interface to perform accurate simulations of flows through 3D multirow geometries [27]. The DA solver was then obtained by differentiating the newly developed multidomain RANS solver and the mixing-plane boundary conditions. Similarly to the work described in [25,26], the method is based on the duality-preserving approach [21] obtained by reformulating the state constraint into a fixed-point problem. This results in an adjoint solver that inherits the same convergence properties of the primal solver.

To test the capabilities of the new design framework, the flow solver was first validated against the experimental results obtained from two conventional turbines whose test cases were available in literature: the Aachen Turbine [28,29], and the single-stage radial turbine of an auxiliary power unit (referred to as the APU turbine in this paper) [30]. Second, the flow solver was also verified against experimental measurements performed on a small radial ORC turbine partially operating in the so-called nonideal compressible fluid dynamic (NICFD) regime [31]. To the authors' knowledge, this

*Researcher.
†Assistant Professor.
‡Full Professor.

represents the first contribution to the open literature reporting the validation of a CFD solver against measurements performed on a mini-ORC turbine. Finally, the adjoint solver, together with the entire optimization framework of SU2, was applied to redesign the Aachen turbine in order to demonstrate the unique capabilities of the auto-mated design procedure.

This paper is structured as follows. Section II focuses on the extension of the SU2 unstructured vertex-based RANS solver to accurately simulate 3D multistage turbomachinery. Section III describes the generalization of the adjoint equations for multiple flow domains. Section IV reports a series of test cases used to validate the solver by comparison with experimental data. Section V documents the redesign of the Aachen turbine using the newly developed DA solver. Concluding remarks and future work are briefly discussed in Sec. VI.

II. Flow Solver

A. Spatial Discretization

The RANS equations are discretized using a finite volume method with a standard edge-based structure on a dual grid with control volumes that are constructed using a median-dual vertex-based scheme [20]. This allows to handle both structured and unstructured grids. The semidiscretized integral form of the governing equations is

$$\int_{\Omega_i} \frac{\partial \boldsymbol{U}}{\partial t}\, d\Omega + \sum_{j \in \mathcal{N}(i)} (\tilde{\boldsymbol{F}}^c_{ij} + \tilde{\boldsymbol{F}}^v_{ij}) \Delta S_{ij} - \boldsymbol{Q} |\Omega_i|$$

$$= \int_{\Omega_i} \frac{\partial \boldsymbol{U}}{\partial t}\, d\Omega + \boldsymbol{R}_i(\boldsymbol{U}) = 0 \qquad (1)$$

where $\boldsymbol{R}(\boldsymbol{U})$ is the residual vector obtained by integrating the source term over the control volume Ω_i and summing up all the projected numerical convective and viscous fluxes $\tilde{\boldsymbol{F}}^c_{ij}$ and $\tilde{\boldsymbol{F}}^v_{ij}$ associated with

the neighboring j nodes to the node i. The residual must be computed for each of the internal and boundary nodes of the flow domain of interest. More details on the spatial discretization can be found in [20].

B. Mixing-Plane Boundary Condition

When multiple-flow domains are coupled via a nonreflecting mixing-plane interface, the computation of the residual over such an interface requires the implementation of a new data structure that allows to access the mesh-nodes information in a span- and pitchwise ordered manner. The spanwise ordering is necessary to impose the mixing-plane condition [32], whereas both orderings are needed to compute the Fourier decomposition of the outgoing characteristic such that quasi-3D nonreflecting boundary conditions (NRBC) can be imposed [33].

The new data structure presented in this work encapsulates the boundary node geometrical data in Cartesian and cylindrical coordinates and contains the information of the particular turbomachinery configuration (i.e., axial and radial) under study. With these two pieces of information, the code automatically 1) selects the spanwise direction in which the mixing-plane layers are computed, and 2) computes the velocity components. For example, in an axial machine (see Fig. 1a) the spanwise levels are computed along the radial coordinate R, and the normal velocity component is parallel to the z axis of rotation. Instead, for a radial cascade (see Fig. 1b), the spanwise bands are computed along the z axis and the normal velocity component is parallel to the radial direction.

Figures 2a and 2b illustrate the fundamentals of the new data structure creation via a piecewise ordering algorithm. First, the number of spanwise bands in which a generic inflow or outflow boundary is discretized is automatically calculated from their intersection with a periodic boundary (cf. Fig. 2a). Once the band levels are determined, the mesh nodes are assigned to the closest band in a pitchwise ordered manner (cf. Fig. 2b).
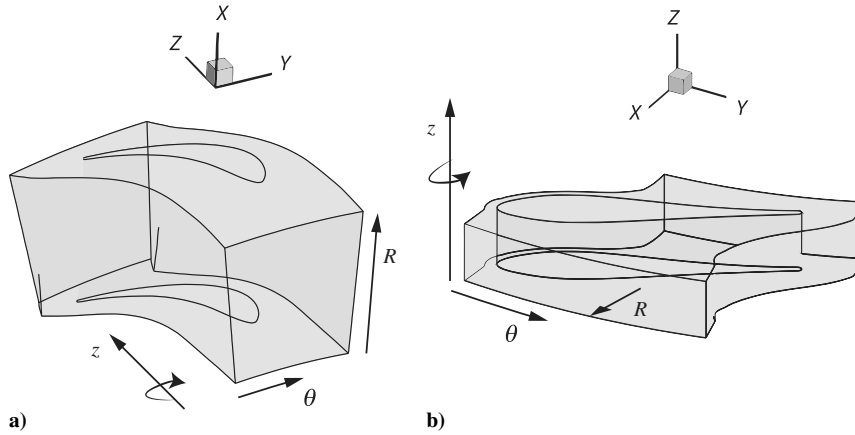

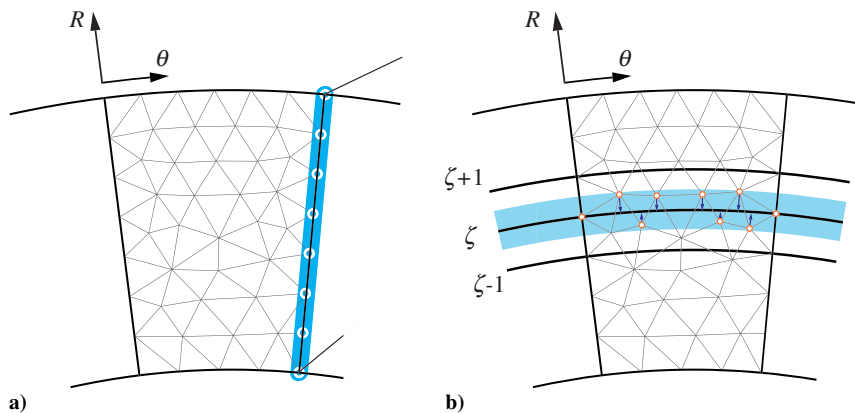Fig. 1   Axial and radial turbomachine flow domain example.

Fig. 2   Node ordering algorithm: a) computation of the spanwise bands; b) allocation of the vertexes to the closest spanwise band.

For each ith node belonging to a specific band level ζ, the characteristic jump is composed by an average and a harmonic component

$$\delta \boldsymbol{c}_{i,\zeta} = \delta \bar{\boldsymbol{c}}_\zeta + \delta \dot{\boldsymbol{c}}_{i,\zeta} \tag{2}$$

The average component $\delta \bar{\boldsymbol{c}}_\zeta$ is the characteristic contribution that ensures that the flow quantities match at the interface. To achieve this objective, the average characteristic jump at each band level is computed as

$$\begin{pmatrix} \delta \bar{c}_1 \\ \delta \bar{c}_2 \\ \delta \bar{c}_3 \\ \delta \bar{c}_4 \\ \delta \bar{c}_5 \end{pmatrix}_\zeta = \begin{bmatrix} -\bar{a}^2 & 0 & 0 & 0 & 1 \\ 0 & 0 & \bar{\rho}\bar{a} & 0 & 0 \\ 0 & 0 & 0 & \bar{\rho}\bar{a} & 0 \\ 0 & \bar{\rho}\bar{a} & 0 & 0 & 1 \\ 0 & -\bar{\rho}\bar{a} & 0 & 0 & 1 \end{bmatrix}_\zeta \begin{pmatrix} \rho^{\text{donor}} - \bar{\rho}^{\text{target}} \\ v_n^{\text{donor}} - \bar{v}_n^{\text{target}} \\ v_\theta^{\text{donor}} - \bar{v}_\theta^{\text{target}} \\ v_\zeta^{\text{donor}} - \bar{v}_\zeta^{\text{target}} \\ p^{\text{donor}} - \bar{p}^{\text{target}} \end{pmatrix}_\zeta \tag{3}$$

where $(\bar{\rho}, \bar{\boldsymbol{v}}, \bar{p})$ are averaged at each spanwise level and $\bar{a}$ is the speed of sound; the target side of the interface is the side in which the boundary condition is actually imposed.

Because in most applications, especially in the presence of tip clearance, the target side and donor side of the interface are discretized with a different number of spanwise levels, the donor quantities on the right-hand side of Eq. (3) are computed using an interpolation algorithm. With a linear interpolation algorithm (cf. Fig. 3), the donor average quantities used in Eq. (3) for the ζth band level are computed using the average quantities of the $(\Psi - 1)$th and Ψth band levels on the donor side. The current mixing-plane interface is conservative with respect to the mass, momentum, and energy fluxes if and only if the primitive variables are averaged using the mixed-out procedure [33].

The harmonic component $\delta \dot{\boldsymbol{c}}_{i,\zeta}$ is calculated using the quasi-3D approach of Saxer and Giles [33], and it prevents the occurrence of nonphysical wave reflections at boundaries. However, with respect to the original work of Saxer and Giles, a modification of the Fourier spatial decomposition is needed in order to take into account the data structure of SU2.

According to the original work of Saxer and Giles, the discrete form of the spatial Fourier transform of a generic outgoing characteristic c_j can be computed as

$$\hat{c}_{j,k,\zeta} = \frac{1}{P} \sum_{i=0}^{n_\zeta - 1} c_{j,i,\zeta} e^{-(2\pi i k/P)y_i} \Delta y_i,$$
$$\text{with } \left(-\frac{n_\zeta}{2} + 1 < k < \frac{n_\zeta}{2} - 1 \right) \tag{4}$$

where P is the pitch length, n_ζ is the number of node per band, k is frequency, Δy_i,

$$\Delta y_i = y_i - y_{i-1} \qquad (i = 1, 2, \ldots, n_\zeta) \tag{5}$$

is the pitchwise distance between two adjacent mesh nodes of the same band, and y_i,

$$y_i = \sum_{m=1}^{i} \Delta y_m \quad \text{with } (i = 1, 2, \ldots, n_\zeta) \tag{6}$$

is the cumulative pitchwise length. However, in the case of unstructured grids, the nodes belonging to the same band do not lie at the same spanwise distance (cf. Fig. 2b); thus, the pitchwise distance between two adjacent nodes becomes less trivial to define.

A more general formulation can be instead obtained by using the coordinate transformation

$$\theta_i = \frac{y_i}{R_i} \tag{7}$$

where θ_i is the cumulative angular distance, which can be computed as

$$\theta_i = \sum_{m=1}^{i} \Delta \theta_m \qquad \text{with } (i = 1, 2, \ldots, n_\zeta) \tag{8}$$

and $\Delta \theta_i$ is the angular distance between two adjacent nodes:

$$\Delta \theta_i = \theta_i - \theta_{i-1} \qquad (i = 1, 2, \ldots, n_\zeta) \tag{9}$$

Using this transformation, Eq. (4) can be reformulated as

$$\hat{c}_{j,k,\zeta} = \frac{1}{P} \sum_{j=0}^{n-1} c_{j,i,\zeta} e^{-(2\pi i k/P)R_i \theta_i} R_i \Delta \theta_i,$$
$$\text{with } \left(-\frac{n_\zeta}{2} + 1 < k < \frac{n_\zeta}{2} - 1 \right) \tag{10}$$

However, because the difference in the spanwise coordinate among the nodes of the same band is generally negligible if compared to the pitchwise length, the dependence of Eq. (4) on R_i can be eliminated, and thus Eq. (4) simplifies into

$$\hat{c}_{j,k,\zeta} = \frac{1}{\theta_{\text{pitch}}} \sum_{i=0}^{n_\zeta - 1} c_{j,i,\zeta} e^{-(2\pi i k/\theta_{\text{pitch}})\theta_i} \Delta \theta_i$$
$$\text{with } \left(-\frac{n_\zeta}{2} + 1 < k < \frac{n_\zeta}{2} - 1 \right) \tag{11}$$

The schematic difference between the two approaches is illustrated in Fig. 4. When unstructured grids are used, the points belonging to the same band level are all projected to the same radial distance. This approximation is not needed when structured grids are employed.
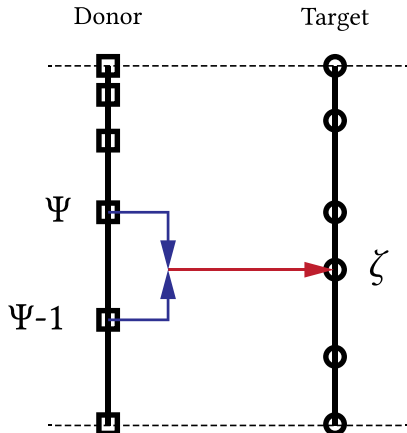

Fig. 3   Schematic view of the interpolation method used at the mixing-plane interface to transfer information from the donor side to the target side.
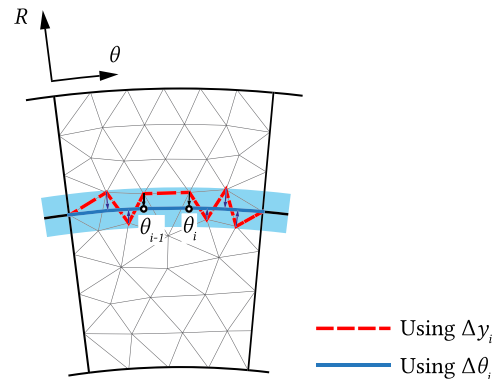

Fig. 4   Schematic illustration of the distance between adjacent nodes using both approaches.

The Fourier decompositions of all the outgoing characteristics of a specific boundary are first linearly combined (according to the 2D nonreflecting theory) and then transformed back into the spatial domain. The result of this procedure gives the harmonic component of Eq. (2).

Once both the average and the harmonic component have been computed, the change of the characteristic variables $\delta c_{i,\zeta}$ is finally converted into a primitive variable perturbation. This perturbation is used to compute the new primitive variables, and in turn the primitive variables are used to compute the numerical convective flux of Eq. (1). The overall procedure is repeated for all the spanwise levels of the boundary.

C. Time Integration

Once the residual vector has been computed, the time integration is performed with an implicit Euler scheme, resulting in the linear system

$$\left(\frac{|\Omega|}{\Delta t^n}\delta_{ij} + \frac{\partial R(U^n)}{\partial U^n}\right)\Delta U^n = -R(U^n) \tag{12}$$

where $\Delta U^n := U^{n+1} - U^n$ and Δt^n is the (pseudo) time step, which may be made different in each cell by using the local time-stepping technique [34]. In the context of multiple flow domains coupled with the mixing-plane interface, the residuals computed in the mixing-plane boundaries depend also on the solution of the adjacent flow domains. In the implementation documented in this paper, this dependency is treated in an explicit manner: the residuals computed at the nth time step in the jth flow domain depend on the solutions of the kth adjacent flow domain computed at the $n - 1$th time step. This can be written as

$$\left(\frac{|\Omega|}{\Delta t^n}\delta_{ij} + \frac{\partial R(U^n)}{\partial U^n}\right)_j \Delta U_j^n = -R(U_j^n, U_k^{n-1}) \tag{13}$$

To ease the implementation, the Jacobian in Eq. (13) is computed by omitting the dependency from the solutions of the adjacent kth flow domain.

III. Discrete Adjoint Solver for Multiple-Flow Domains

The DA method applied to multistage turbomachinery problems involves the generalization of the DA equations for single flow domain to multiple domains, coupled through a steady mixing-plane interface. Following the work presented in [25], let J be the objective function or a constraint of a multistage turbomachinery design problem in which the flow solution is obtained by solving the RANS equations on N multiple-flow domains. Assume that the goal of the optimization problem is to find the minimum of the objective function. If the mesh and surface deformation are performed with linear elasticity equations [35] and free-form deformation (FFD) algorithm [36], the optimization problem can be written as

$$\min_D J[U_1(D), X_1(D_1), \ldots, U_N(D), X_N(D_N)] \tag{14}$$

$$\text{s.t. } U_k = G_k(U, X_k), \qquad \text{with } k = 1, 2, \ldots, N \tag{15}$$

$$X_k = M_k(D_k), \qquad \text{with } k = 1, 2, \ldots, N \tag{16}$$

with

$$D = \{D_1, D_2, \ldots, D_N\} \tag{17}$$

$$U = \{U_1, U_2, \ldots, U_N\} \tag{18}$$

D_k represents the design variables used to deform the blade in the kth domain, and U_k and X_k are the respective flow solution and mesh of the same domain. While X_k depends only on the design variables that act on the kth domain, U_k, as shown in Eq. (15), is influenced by the

solutions of the other flow domains through the mixing-plane interface [cf. Eq. (13)] and, as such, by the entire vector of design variables (D). As for the single-flow-domain case [25], M_k is a linear function that represents the mesh and surface deformation, and G_k is the flow solver iteration. Differently from the single-flow-domain case, N constraints on the flow solution, Eq. (15), and on the surface and volume deformation iterative process, Eq. (16), must be imposed to ensure that convergence is reached in any of the flow domains for both the flow solver and the mesh deformation process.

The Lagrangian associated to this problem can be then expressed as

$$L(D, U, X, \bar{U}, \bar{X})$$
$$= J(U, X) + [G_1(U, X_1) - U_1]^T \bar{U}_1 + \ldots + [G_N(U, X_N) - U_N]^T \bar{U}_N$$
$$+ [M_1(D_1) - X_1]^T \bar{X}_1 + \ldots + [M_N(D_N) - X_N]^T \bar{X}_N, \tag{19}$$

where $\bar{X}_k$ and $\bar{U}_k$ are arbitrary Lagrange multipliers. Differentiating L with respect to each D_k, and by choosing each $\bar{X}_k$ and $\bar{U}_k$ in such a way that the terms $(\partial U_i/\partial D_k)$ and $(\partial X_i/\partial D_k)$ can be eliminated, leads to N adjoint equations

$$\bar{U}_k = \frac{\partial}{\partial U_k}J^T(U, X) + \sum_{i=1}^{N}\frac{\partial}{\partial U_k}G_i^T(U, X_i)\bar{U}_i,$$
$$\text{with } k = 1, 2, \ldots, N \tag{20}$$

and to N mesh sensitivity equations

$$\bar{X}_k = \frac{\partial}{\partial X_k}J^T(U, X) + \frac{\partial}{\partial X_k}G_k^T(U, X_k)\bar{U}_k,$$
$$\text{with } k = 1, 2, \ldots, N \tag{21}$$

Once all the adjoint solutions $\bar{U}_k$ have been computed, the mesh node sensitivity at each flow domain $\bar{X}_k$ is computed by evaluating Eq. (21), and, finally, the N total derivatives of J with respect to the design variables of each kth domain are given by

$$\frac{dJ^T}{dD_k} = \frac{d}{dD_k}M_k^T(D_k)\bar{X}_k, \qquad \text{with } k = 1, 2, \ldots, N \tag{22}$$

As for the method described in [25], the derivatives $(\partial J/\partial U_k)$, $(\partial J/\partial X_k)$, $(\partial G_i/\partial U_k)$, $(\partial G_k/\partial X_k)$, and (dM_k/dD_k) are computed by resorting to the reverse mode of the open-source algorithmic differentiation tool CodiPack [21,22].

IV. Validation of the RANS Solver

The newly developed RANS solver for multirow turbomachinery simulations of compressible flows was validated by comparing simulation results to experimental data related to three turbine test cases documented in the literature. The first test case considered is referred to as *Aachen turbine* and consists of a one-and-half stage of an axial turbine that was conceived and realized in order to provide data sets for turbomachinery code validation [28]. The second test case is a single-stage radial turbine of an auxiliary power unit (here referred to as the *APU turbine*) [30]. The third validation test case is a single-stage radial ORC turbine designed for small-scale applications [37]; thus, it is termed *mini-ORC turbine* in the following.

A. Aachen Turbine

The three flow domains of the Aachen turbine (i.e., stator 1, rotor 1, and stator 2) were discretized using structured grids generated with a commercial software [38]. The grid comprises a total amount of 5 million elements, after a mesh independence study. The turbulence effects are modeled using the k–ω Shear-Stress-Transport (SST) turbulence model [39], and a full resolution of the boundary layer was obtained by ensuring wall $y+ < 1.0$ at the blades and at the hub and shroud surfaces. The spanwise values of the quantities imposed
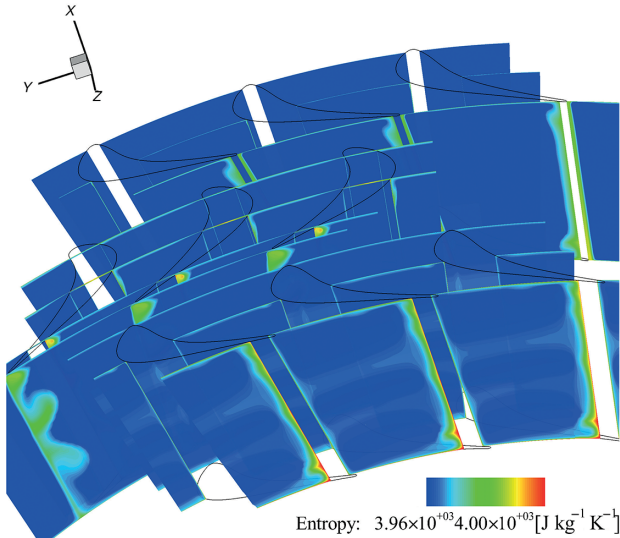
Fig. 5   Entropy contour of the Aachen turbine.

Table 1   Fluxes relative error across the mixing-plane stator–rotor and rotor–stator interfaces

Fluxes relative error	Stator 1–rotor	Rotor–stator 2
F_ρ	8.8E − 04	9.2E − 04
F_{v_n}	2.0E − 05	8.2E − 06
F_{v_t}	8.6E − 04	1.6E − 03
F_k	3.5E − 03	4.8E − 03
F_ω	1.5E − 03	1.2E − 02

as boundary conditions at the inlet of the first stator (i.e., total pressures, total temperatures, flow directions) and at the outlet of the second stator (static pressures) are the ones corresponding to the reported experimental data with lower mass flow rate [28].

The convective terms are discretized using a Roe upwind scheme [40] for which second-order accuracy is achieved with the MUSCL reconstruction, whereas the viscous terms are discretized using the average-gradient formulation. For both fluxes, the gradients are evaluated using a least-squares method [41]. A convergence rate of six orders of magnitude on both the flow and turbulent quantities was achieved in 2000 iterations using an Euler implicit time-marching scheme with a Courant–Friedrichs–Lewy (CFL) number of 20 without multigrid.

Figure 5 shows the entropy distribution on different secondary planes in the streamwise direction. As expected, the largest entropy

generation occurs on the suction side of each blade rows. The appearance of the tip clearance vortex at the tip of the rotor cascade is also evident. Although the tip vortex is averaged out by the mixing-plane interface between the rotor and the second stator, the spanwise flow distribution at the inlet of the second stator remains highly nonuniform, resulting in larger secondary flow losses if compared with the ones occurring in the first row.

Table 1 shows that the mixing-plane algorithm, implemented following the method described in Sec. II, is capable of conserving the overall fluxes across the two interfaces. The fluxes are conserved even along the spanwise direction, proving the full conservative property of the mixing-plane method.

The results obtained with SU2 were compared with the experimental data and to the flow simulation results obtained with other RANS solvers (i.e., TFLOW, 3DFLOW, APNASA-V5) reported in the work of Yao et al. [42]. Figures 6a and 6b show the absolute flow angle and total-pressure spanwise distributions predicted by all these CFD tools and those measured at the interface between the rotor and second stator. Figures 7a and 7b display the same quantities at the outlet section of the second stator. It can be observed that the SU2 predictions are generally in good agreement with the quantities calculated with the other flow solvers for what concerns the flow angle distribution, but they are closer to the experimental data with regard to the spanwise trend of the total pressure.

B.   APU Turbine

The geometry of the APU turbine was reconstructed using the information provided by Sauret [43] and adopting the method proposed by Verstraete [44]. Because no information was given with respect to the shape of the spinner, an elliptical spinner was used because it facilitates the convergence of the simulations. Figure 8 shows the meridional section of the turbine.

After a grid convergence study, the three flow domains (i.e., stator, rotor, and diffuser) were discretized using structured grids for a total amount of 3 million elements. The selected turbulence model was the k–ω SST [39], and $y+ < 1.0$ was ensured at the wall boundaries. The boundary conditions selected for this test case are the ones corresponding to the 5.7 pressure ratio of the experimental campaign [30] and are shown in Table 2. The convective terms were discretized using a second-order Roe upwind method whereby the monotonicity of the scheme is ensured by applying the Van Albada limiter [45]. The viscous terms are discretized using the average-gradient formulation, and the gradients are computed using a least-squares method. A reduction of five orders of magnitude on both the flow and turbulent residuals was obtained in 3000 time steps using an implicit Euler scheme with a CFL number of 20. To guarantee a smooth convergence, the rotational speed was linearly increased from zero to the final value during the first 500 iterations.

The entropy contours at different streamwise locations are shown in Fig. 9. As expected, the highest fluid dynamic losses take place on the suction side of the rotor due to the presence of a large tip-clearance
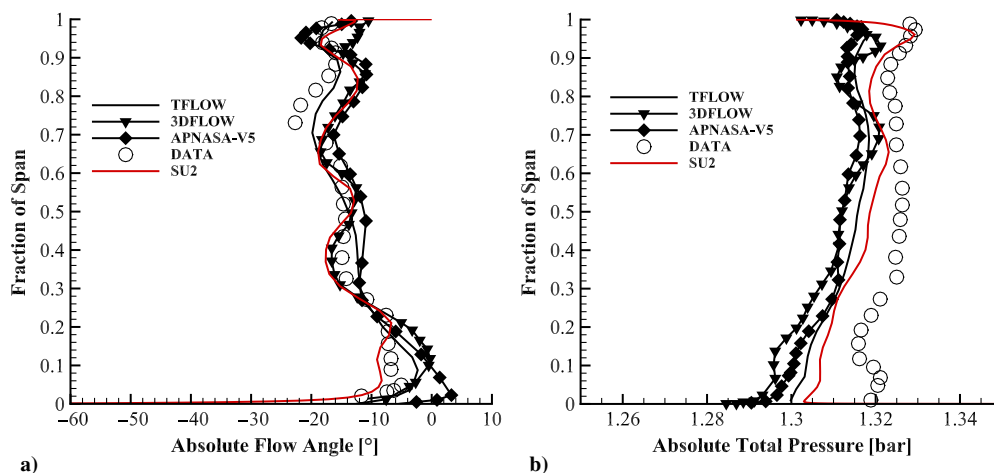

Fig. 6   Properties distribution at the stator 1–rotor interface: a) absolute flow angle; b) total pressure.
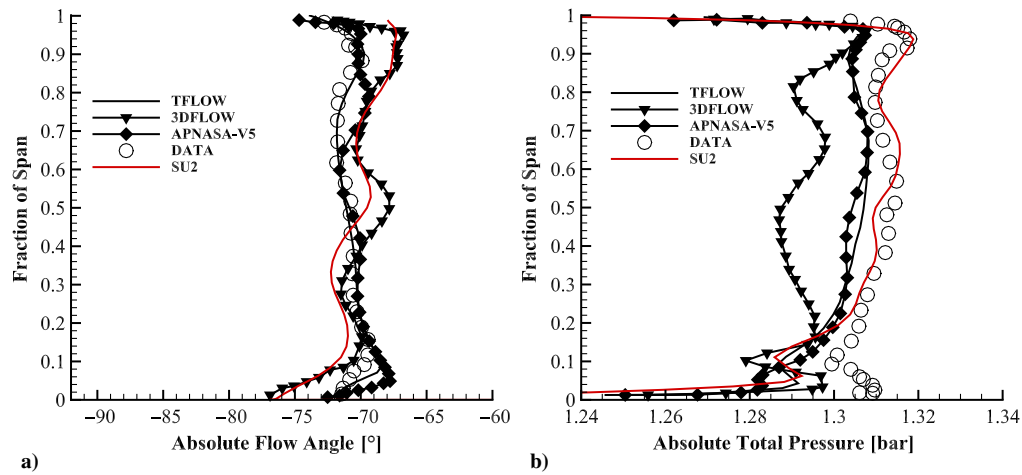
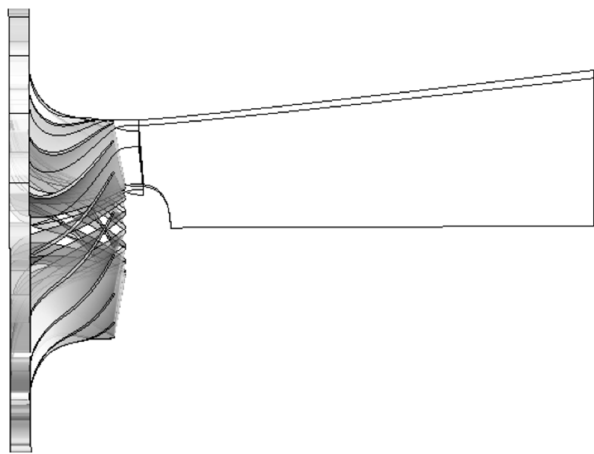**Fig. 7 Properties distribution at the rotor–stator 2 interface: a) absolute flow angle; b) total pressure.**

Fig. 8 Meridional view of the APU turbine.

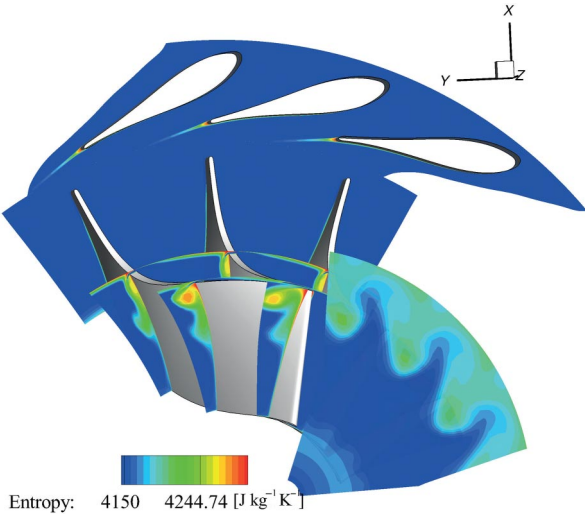Entropy: 4150 4244.74 [J kg⁻¹ K⁻¹]

Fig. 9 Entropy contour of the APU turbine.

vortex. Because of dissipation, the intensity of the vortex is then reduced within the diffuser generating additional mixing losses. Additionally, a large area of flow separation is visible at the center of the diffuser because of the abrupt increase of passage area.

The variation of the total to static efficiency with respect to the rotational speed for a constant expansion ratio value is shown in Fig. 10. The CFD results were obtained by varying the rotational speed from 85 to 110% of its nominal value, which corresponds to a specific speed of $u/v_{ax} = 0.7$. The results show that SU2 is capable of reproducing the experimental trend and of correctly computing the point of maximum efficiency, which corresponds to $u/v_{ax} = 0.75$. An absolute difference that varies from 0.5 to around 2% is observed between the measurements and the CFD predictions. This deviation monotonically increases from lower to higher specific speeds. This can be arguably attributed to the averaging of quantities that is inherent to the modeling of the rotor–stator flow interface by means

of the mixing-plane method. As shown in Fig. 11, at lower specific speeds the flow becomes highly transonic and comparatively more nonuniform at the outlet of the stator. The use of the mixing-plane interface results in the simulation of a less dissipative flow, leading to the calculation of a higher rotor performance and eventually to the

Table 2 Inlet and outlet boundary condition values for the APU turbine test case

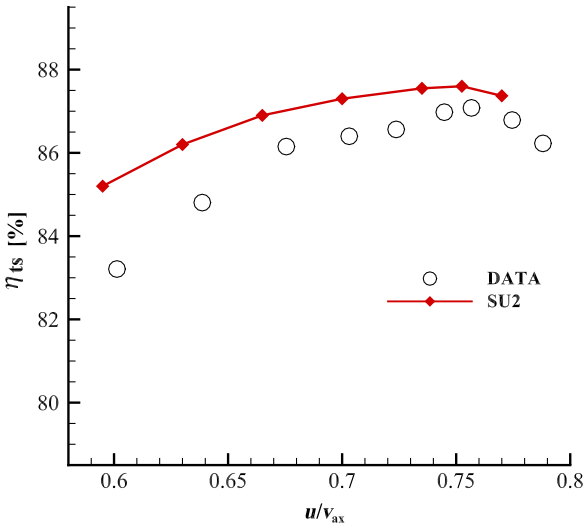|	
$T_{tot,in}$	477.6 K
$p_{tot,in}$	413.6 kPa
β_{in}	0.0°
p_{out}	72.4 kPa
Ω	71,700 rpm
$I_{tur,in}$	0.05
$(\mu_{tur}/\mu_{lam})_{in}$	100.0

Fig. 10 Comparison between numerical and experimental data of the total static efficiency of the machine for different rotational speeds.

a) $u/v_{ax} = 0.6$
M: 0.1 0.3 0.6 0.8 1.1

b) $u/v_{ax} = 0.70$
M: 0.1 0.3 0.6 0.8 1.1
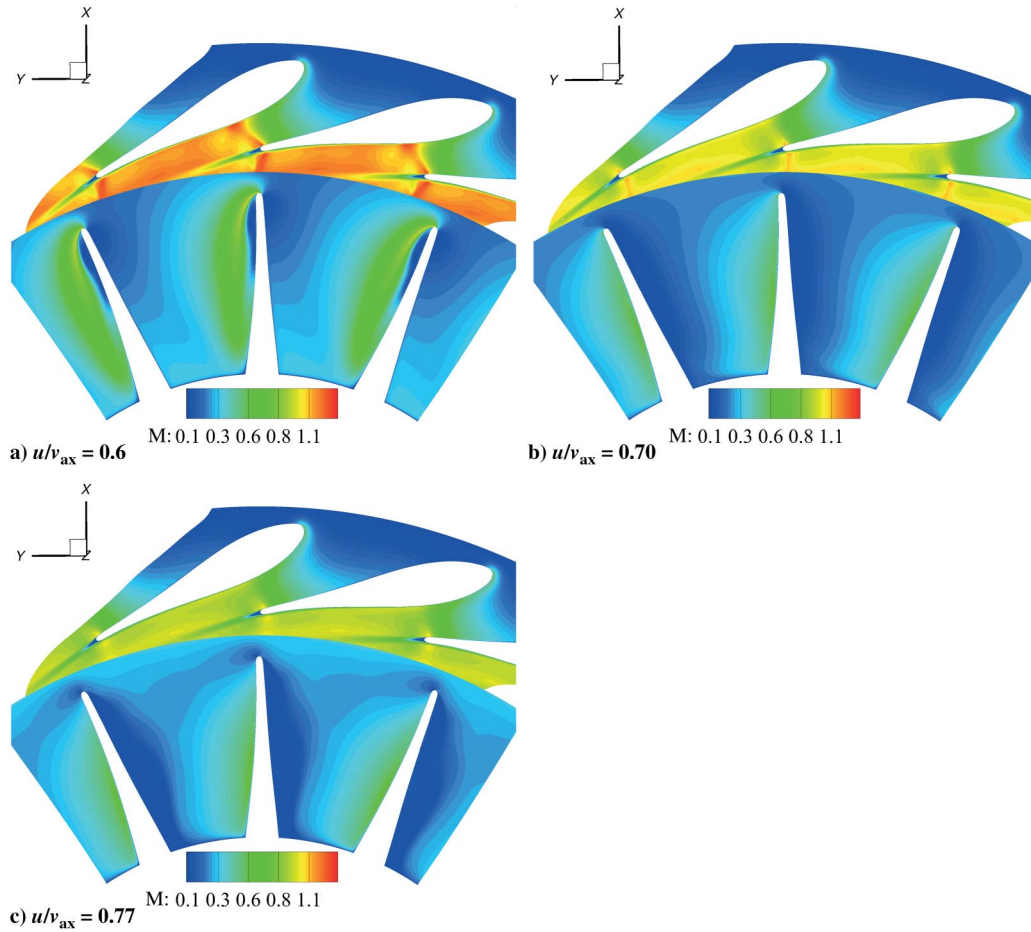
c) $u/v_{ax} = 0.77$
M: 0.1 0.3 0.6 0.8 1.1

Fig. 11 Mach number contour at the stator–rotor interface of the APU turbine for different rotational speeds.

overestimation of the turbine total-to-static efficiency, especially at lower specific speed. Similar conclusions about the diffusivity of the mixing-plane interface in the presence of transonic flows are also reported in other works in the literature [46]. The accuracy of the flow solver of SU2 is also confirmed by the comparison of the averaged flow kinematic quantities measured and computed at the stator and rotor outlet sections (cf. Table 3).

Finally, Fig. 12 shows the comparison between the numerical and experimental values of the absolute flow angle along the spanwise direction at the inlet section of the diffuser. Overall, the CFD results are in accordance with the experimental trend with the exception of the tip region. In the absence of additional information on measurements uncertainty, the results are deemed satisfactory for the purpose of this study.

C. Mini-ORC Turbine

The geometry and experimental results of the mini-ORC turbine test case were provided to the Propulsion and Power group of Delft University of Technology by an industrial partner for the purpose of validating the SU2 flow solver in case of turbomachinery operating in the nonideal flow regime, that is, the flow regime in which the fluid thermophysical properties cannot be calculated by the perfect gas

law. The geometry, together with the experimental results and boundary conditions of the turbine, is confidential; thus, certain information in the description of this test case is omitted, and the results presented are all scaled by means of undisclosed factors.

The machine is a radial inflow ORC turbine operating with an organic compound as working fluid. The flow simulation encompasses three single-passage domains, namely, a stator, a rotor, and a rectilinear outlet region; the turbine was discretized using structured grids. The selected turbulence model was the k–ω SST [39], and $y+ < 1.0$ was ensured at the wall boundaries. Given the highly

Table 3   One-dimensional averaged
kinematic quantities at the stator and
rotor outlet sections

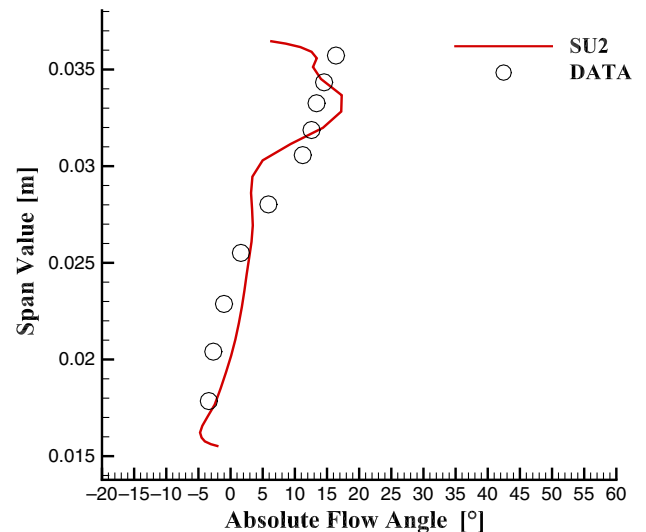| Quantity	DATA	SU2	Error, %
$\alpha_{out,stator}$, °	77.7	77.9	0.02
$M_{out,stator}$	0.985	0.982	0.3
$\beta_{out,rotor}$, °	56.1	56.8	1.2
$Mr_{out,rotor}$	0.71	0.72	1.4

Fig. 12   Comparison between numerical and experimental data of the absolute flow angle along the spanwise direction at the outlet section of the rotor.
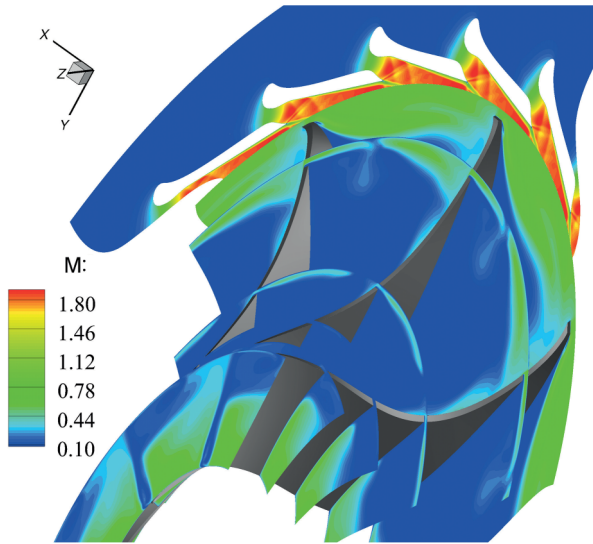
Fig. 13   Mach contour of the mini-ORC turbine.

supersonic flow regime in both the stator and the rotor passages and the severe flow separations on the rotor blade arguably due to sub-optimal impeller blade design, a fully converged steady-state solution was obtained by using the first-order upwind generalized Roe scheme [47] for the convective terms [48] while second-order accuracy was maintained for the viscous terms. Mesh independence studies resulted in a grid composed by about 5 million elements (1.5 million for the stator, 3 million for the rotor, 0.5 million for the outlet). Thermodynamic quantities are computed using the Peng–Robinson equation of state [48]. A reduction of five orders of magnitude on both the flow and turbulent residuals was obtained in 5000 time steps using an implicit Euler scheme with a CFL number of 10. To guarantee a smooth convergence, the rotational speed was linearly increased from zero to the final value during the first 1500 iterations.

Figure 13 shows the Mach contours at different streamwise locations for the turbine working in nominal condition ($\Omega = 1$). As evident, a large region of flow separation occurs at the inlet of the rotor due to incidence effects. The misalignment between the flow angle and the blade inlet angle along with the blunt shape of the leading edge causes an expansion fan on the front suction side of the impeller followed by a shock wave.

Figure 14 shows the variation of the normalized efficiency with respect to the normalized rotational speed for a constant expansion ratio; reported values are calculated from simulations and from measurements for comparison. The Mach contours associated to the four validation points are shown in Fig. 15. The results show that
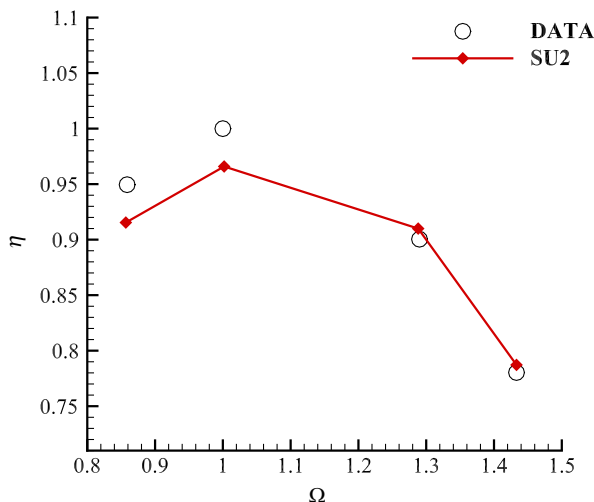

Fig. 14   Comparison between numerical and experimental data of the efficiency of the machine for different rotational speeds.

SU2 is capable of reproducing the measured trend and of correctly predicting the point of maximum efficiency. However, a deviation of few percentage points is observed between the experimental and the CFD results. The deviation may be attributed to the use of the first-order approximation for the discretization of the convective terms. In the absence of additional information on measurements uncertainty, the results are deemed satisfactory and they document, for the first time to the authors' knowledge, that standard RANS CFD solvers equipped with specialized numerical schemes and sufficiently accurate fluid thermophysical models can be used to predict the fluid dynamic performance of mini-ORC turbines at on- and off-design conditions.

V.   Application of the RANS Adjoint Solver

The capabilities of the multiple-flow-domain RANS adjoint solver described in Sec. III were assessed by performing the numerical optimization of the fluid dynamic performance of the Aachen turbine. First, the gradient validation is documented: the adjoint sensitivities of the objective function are compared with that calculated with finite differences. The results of the optimization are then presented. Finally, the impact of the constant eddy viscosity (CEV) approximation on the accuracy of the gradient is reported and discussed.

A.   Aachen Optimization

To improve the simulated performance of the Aachen turbine, the entropy generation, defined as

$$s_{\text{gen}} = \frac{T_{\text{tot,in}}}{v_{\text{spout}}^2} \sum_{k=1}^{3} (s_{\text{out}} - s_{\text{in}})_k \qquad (23)$$

was minimized under the constraint that the shaft power is kept constant, together with the outlet flow angle of the second stator. The constraint on the flow angle ensures that the optimizer does not converge on a solution in which the second stator is flattened.

Because the purpose of this study is just to prove the capability of the optimization framework, a coarser mesh was adopted in order to reduce the computational cost. The new mesh comprises 600,000 grid points with no boundary-layer discretization at the shroud and the hub surfaces. Consequently, a free-slip boundary condition was applied to the end walls. Except for this, the other boundary conditions and all the other options were kept the same as for the validation of the RANS flow solver described in Sec. IV.A.

The deformation of the blades was obtained using as design variables the tangential displacement of the control points of three cylindrical free-form deformation (FFD) boxes (one box per blade), as can be seen in Fig. 16. The FFD boxes used for the optimization are of degree 6 in both the tangential and axial direction and degree 3 in the radial direction. This results in a total amount of 588 design variables (196 per each blade). To avoid unfeasible designs, the trailing edges were excluded from the FFD boxes. Nonetheless, continuity up to the second-order derivative was guaranteed at the intersection between the blade and the boxes.

With regard to computational cost, it was found that the run time per iteration of the adjoint solver is on average 30% higher than the one of the direct solver, and it required about four times more memory usage.

1.   Gradient Validation

The validation of the gradient for all the 588 design variables is computationally prohibitive because it requires 589 solutions of the direct solver to compute the sensitivity using first-order finite difference scheme. Therefore, the sensitivity is validated with respect to the control points of three FFD boxes of degree one in each direction. This corresponds to 24 design variables in total (8 for each blade). Furthermore, because the DA algorithm is independent from the parameter with respect to which the sensitivity is computed (as described in Sec. III), the validation process is hereafter presented only for the entropy generation parameter. Finally, a nondimensional step size equal to 1E − 05 was used for the finite difference algorithm.

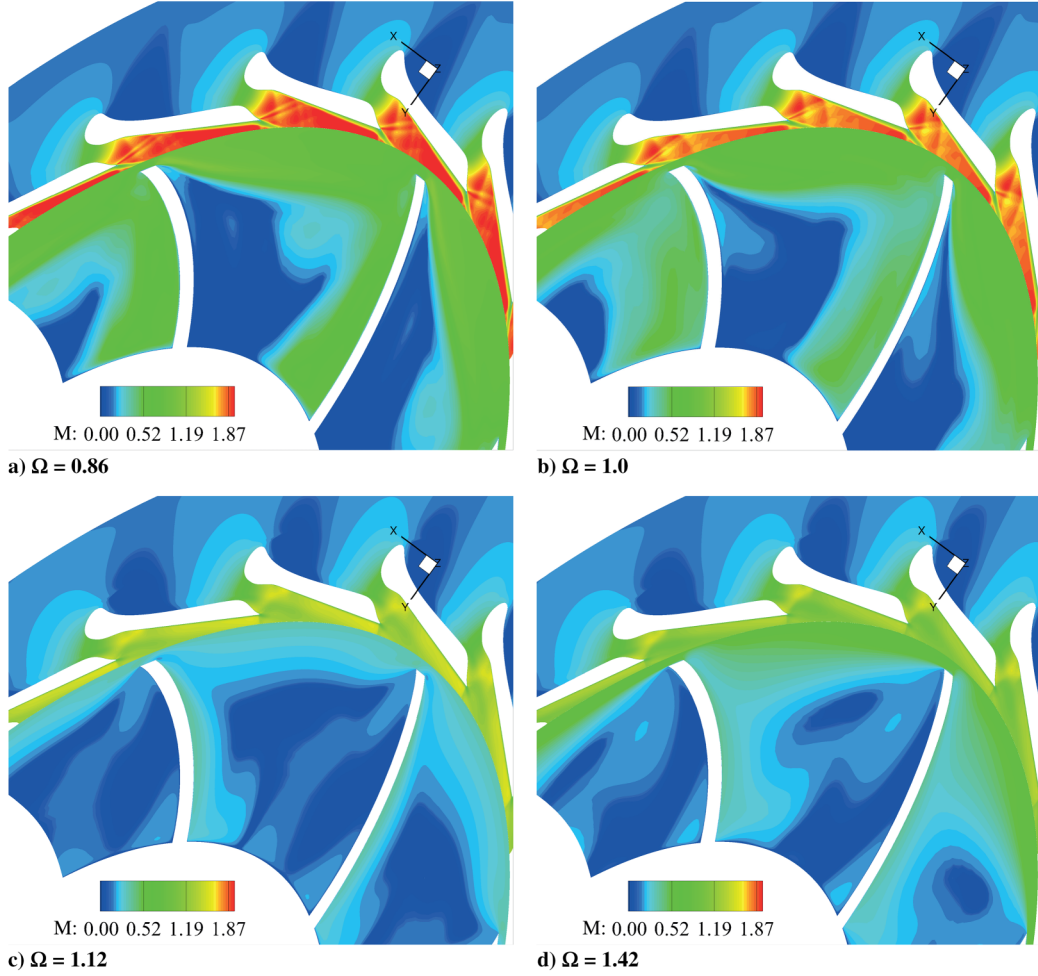a) $\Omega = 0.86$ b) $\Omega = 1.0$ c) $\Omega = 1.12$ d) $\Omega = 1.42$

Fig. 15 Mach number contour at the stator–rotor interface of the mini-ORC turbine for different rotational speeds.

Fig. 16 FFD boxes for the Aachen test case.
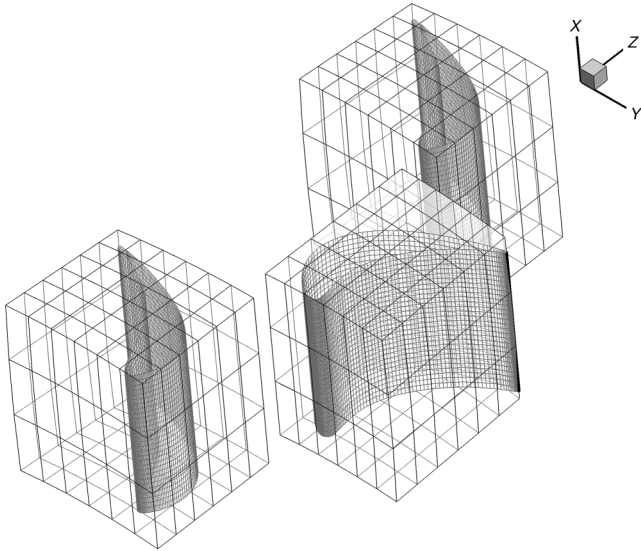

Fig. 17 Convergence history of the RANS adjoint solver for the Aachen turbine test case.

Figure 17 shows the convergence history of the density adjoint residuals $R_{\rho,k}$ for each flow domain and the convergence of the overall geometrical sensitivity, computed as

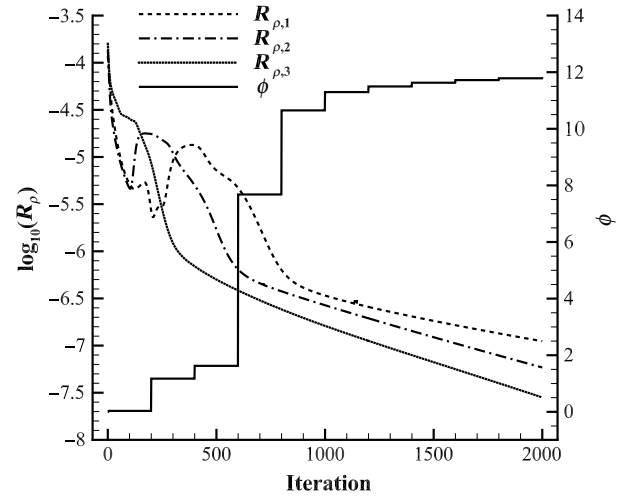$$\phi = \sum_{k=1}^{3} \|\bar{X}_{k,\text{blade}}\| \qquad (24)$$

where $\bar{X}_{k,\text{blade}}$ is the mesh sensitivity projected over the blade surface of each row. The overall geometrical sensitivity, although the adjoint residuals drops of only about three orders of magnitude, converges rapidly to its final value. The calculation of ϕ at each iteration is computationally demanding, because it requires the evaluation of Eq. (21) at each time step. Hence, ϕ is calculated only at certain time steps (in this case every 200 iterations) only for the sake of monitoring the gradient convergence.
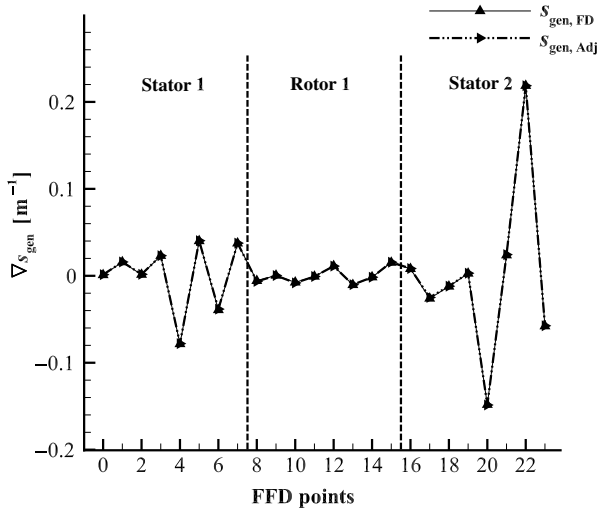
Fig. 18   Validation of the entropy generation gradient obtained with the discrete adjoint against the one computed with the finite difference scheme for the Aachen turbine.
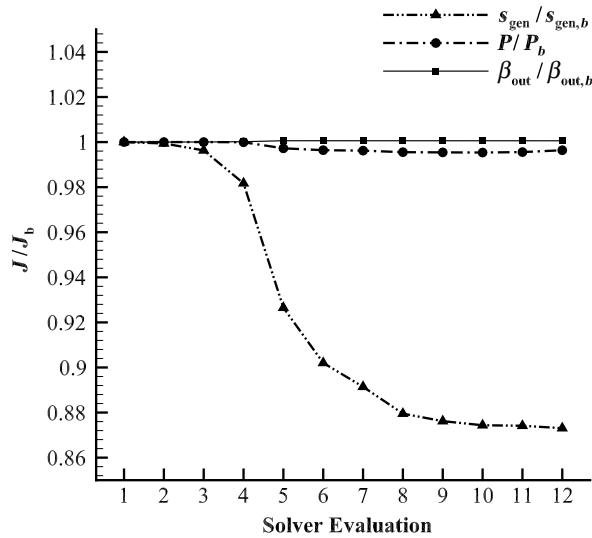

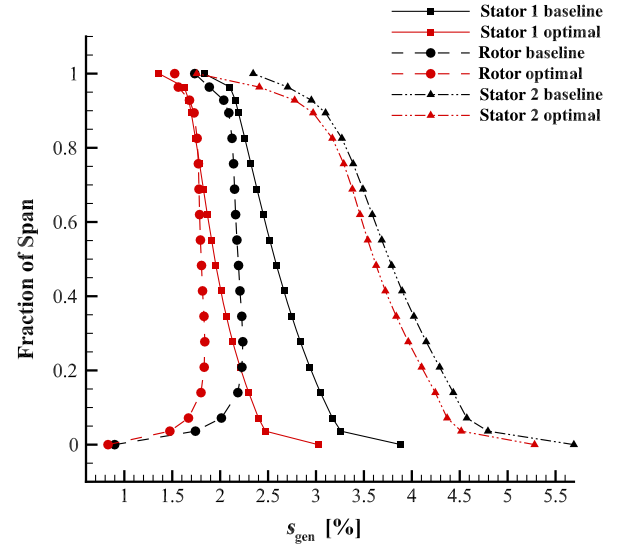Fig. 19   Optimization history for the Aachen turbine test case.

Fig. 20   Spanwise value of the entropy generation parameter computed for each row for both the optimal (red) and the baseline (black) geometries.
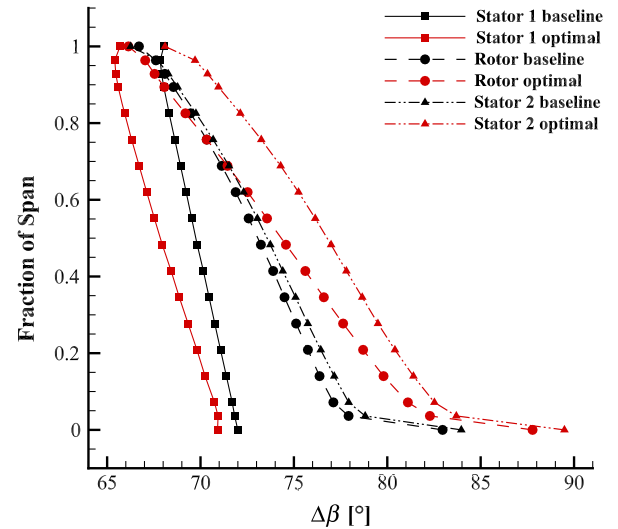

Fig. 21   Spanwise value of the flow deflection of each blade row for both the optimal (red) and the baseline (black) geometries.

As depicted in Fig. 18, the gradient of the entropy generation provided by the DA very accurately correlates with the one obtained with finite differences. This confirms that all the components of the RANS flow solver and mesh deformation routines (cf. Sec. III) were correctly differentiated, including the turbulence model and the mixing-plane boundary conditions.

2. Optimization

The normalized optimization history in Fig. 19 shows that the sequential least squares programming (SLSQP) [49] algorithm converges in 10 iterations, achieving a total entropy generation reduction of 12%, whereas the total-to-total efficiency increases by as much as 3%. The equality constraints of power, denoted as P/P_b in the figure, and outlet flow angle $\beta/\beta_{out,b}$ are satisfied with differences of 0.4 and 0.05% with respect to their prescribed values.

Figure 20 depicts the spanwise distribution of the entropy generation performance parameter for each row for both the baseline and the optimal geometry. The figure shows that the optimization method enables the reduction of the fluid dynamic losses along the entire span of each blade. The spanwise flow deflections of the optimal and baseline blades are presented in Fig. 21; both the optimal and the baseline turbine configurations feature a monotonic decrease of the blade loading along the span direction. In spite of the increased blade

loading, the optimal rotor and second stator exhibit lower fluid dynamic losses.

The 2D sections of the blades at the hub, mid, and shroud for both the optimal (red) and the baseline (black) are presented in Fig. 22. In each of the rows, the optimal solution contains more slender blade profiles, which led to a reduction of profile losses. In addition, the optimal blades are more slender along the blade span. This trend is more pronounced for the rotor and second stator blades as they present a larger difference in blade loading along the span. The integral views of the 3D optimal and baseline blade shapes are shown in Fig. 23.

B. Assessment of the Constant Eddy Viscosity Approximation

Because a wide body of work concerning adjoint methods reported in the literature is based on the so-called CEV approximation [19], it is of practical interest to evaluate if the adoption of such approximation may lead to satisfactory results. To this purpose, the adjoint solutions of the Aachen turbine and the APU turbine computed with and without the CEV approximation are presented and discussed. The two test cases are simulated using the same operating conditions as those reported in Sec. IV; the sensitivity of the entropy generation
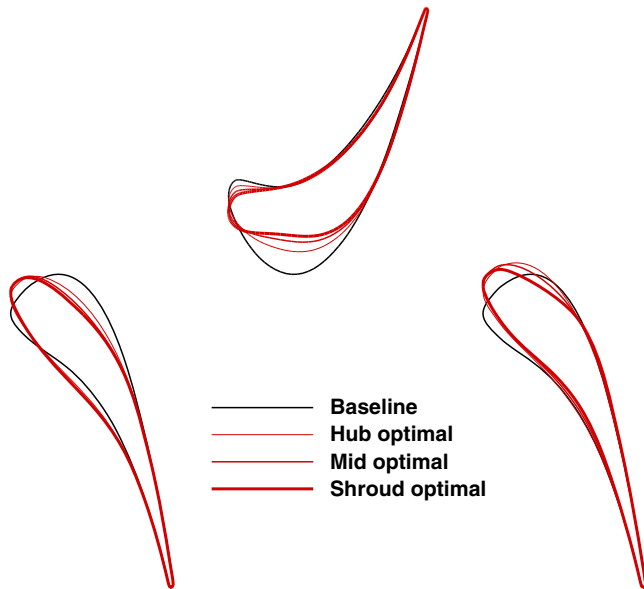
Fig. 22 Comparison of the 2D sections at the hub, mid, and shroud span of the optimal blade shapes (red) with respect to the baseline geometries (black). The baseline is represented by one single continuous black line as the blades are prismatic.
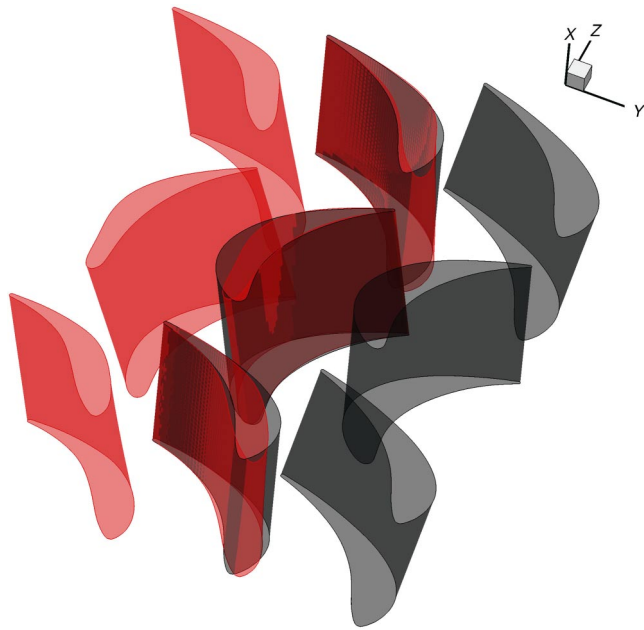

Fig. 23 Comparison between the optimal 3D blade shapes (red) and the baseline geometries (black).

performance parameter [cf. Eq. (23)] is computed with respect to the tangential component of the FFD box points. Each blade was enclosed within an FFD box of degree one in each direction, namely, eight degrees of freedom per blade.

Figure 24 shows the comparison between the sensitivities computed with and without the CEV approximation for the Aachen test case. The use of the CEV approximation leads to considerable accuracy errors for the stator 1 and rotor 1 sensitivities, whereas the error related to the second stator is lower. This deviations can be directly connected to the flow regime in which the blades operate. As illustrated in Fig. 25, the first two blades operate always in highly subsonic conditions (Mach number below 0.5), whereas larger values of Mach number are calculated for the last blade. The same behavior is observed for the APU turbine. In this case, the CEV approximation has a lower impact on the accuracy of the computed sensitivity
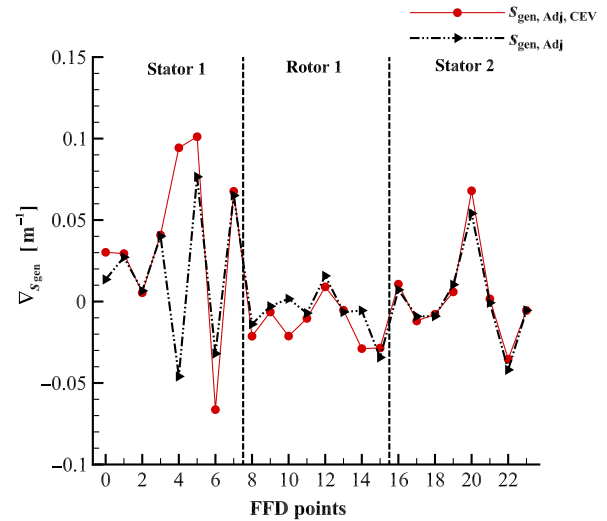

Fig. 24 Comparison between the sensitivities computed with and without the CEV approximation for the Aachen test case.
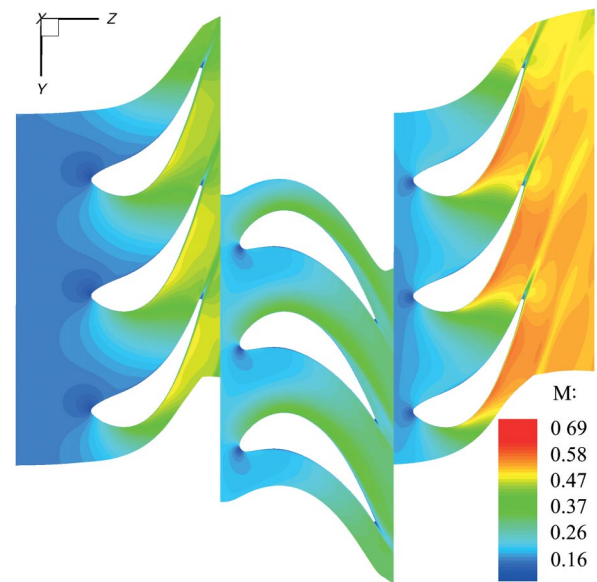

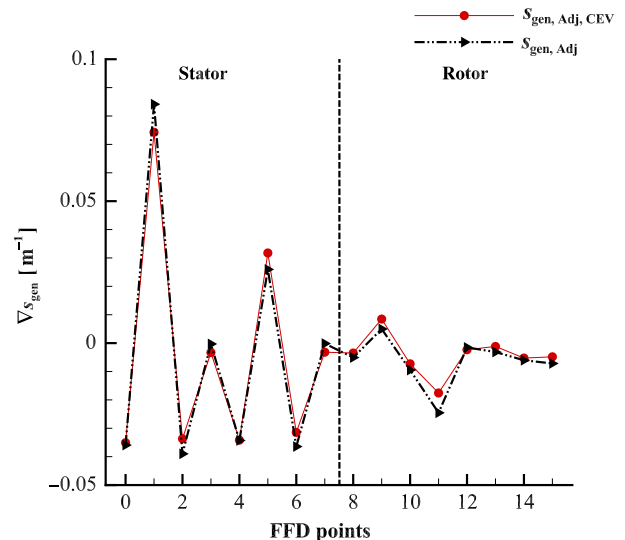Fig. 25 Blade to blade Mach contour of the Aachen turbine.

Fig. 26 Comparison between the sensitivities computed with and without the CEV approximation for the APU test case.
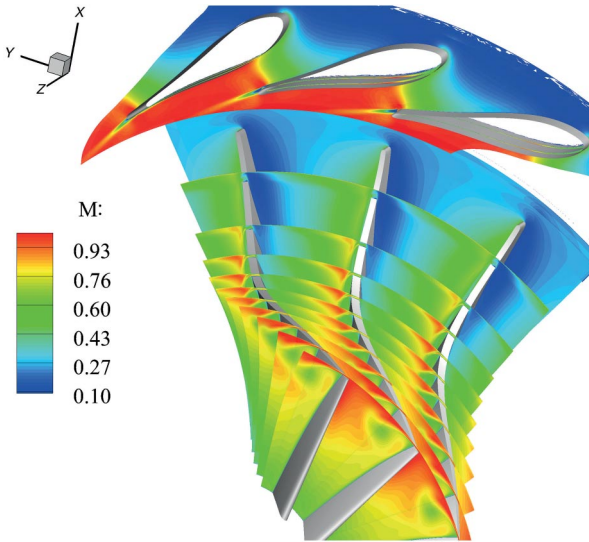
Fig. 27　Mach contour of the APU turbine.

(cf. Fig. 26) as the entire turbine operates mainly in transonic conditions (cf. Fig. 27).

To demonstrate the dependency of the accuracy of the CEV approximation on the flow regime, a 2D cascade is simulated for different expansion ratios (from subsonic to transonic conditions). For each condition, the average error of the computed sensitivity is calculated using the CEV approximation with respect to the case in which the Spalart–Allmaras (SA) [50] and k–ω SST [39] turbulence model are included in the derivation of the adjoint equations. Figure 28 shows the Mach contours of the simulated cascade and the estimated error for the use of the CEV approximation at the various pressure ratios. As anticipated, larger errors are encountered at low Mach numbers, and the error monotonically decreases with the increasing Mach number. Unsurprisingly, as the SST turbulence model is a more complex model than the SA one, the use of the CEV approximation leads to higher errors for the case in which the turbulence phenomena are described with the SST model as also shown in Fig. 28b.

From these findings, it can be inferred that the CEV approximation adopted, for example, in recent works [18,51], can provide accurate results for transonic or supersonic turbomachinery applications, although it is debatable whether it allows to achieve sufficient accuracy for the optimization problem in which cascades operate at low Mach numbers. However, it remains an open question whether the CEV approximation is acceptable in multirow unsteady optimization problems in which wake–rotor interaction plays an important role.

VI.　Conclusions

This paper documents the extension and validation of the RANS flow and adjoint solver of the open-source CFD platform SU2 to the simulation and automated fluid dynamic optimization of 3D multirow turbomachinery. The flow solver was enriched with a conservative and nonreflecting mixing-plane interface, and the DA solver was obtained by resorting to automatic differentiation. A multiple-flow-domain, fully turbulent DA solver was obtained by resorting to an operator-overloading algorithmic differentiation tool, called CoDiPack. The validation highlighted that the gradient provided by the DA very accurately correlates with the one obtained with finite differences.

The accuracy of the flow solver was assessed by comparison with measurements related to two reference gas turbines and to a mini-ORC turbine operating with a highly supersonic stator in the NICFD regime. The results showed that the SU2 RANS flow solver was able to accurately simulate the flow of two standard turbine test cases that
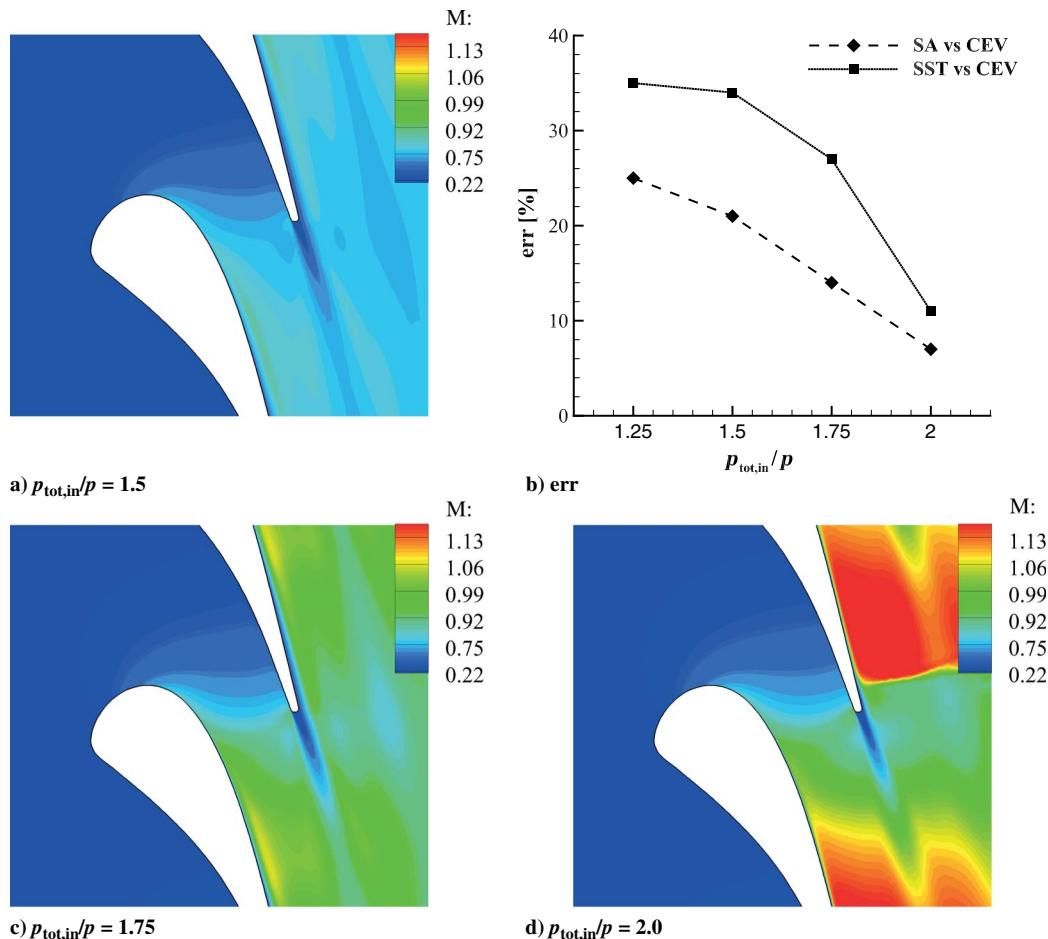

a) $p_{tot,in}/p = 1.5$

b) err

c) $p_{tot,in}/p = 1.75$

d) $p_{tot,in}/p = 2.0$

Fig. 28　Mach number contour at the stator–rotor interface of the mini-ORC turbine for different rotational speeds.

are representative of industrial practice. More in particular, the tool is capable of predicting flow quantities with the same level of accuracy of other RANS solver already reported in the literature. The analysis made on the mini-ORC turbine also revealed that the solver can accurately predict the speed line of such unconventional turbine operating partly in the NICFD regime. To the authors' knowledge, this is the first contribution to the open literature in which a CFD solver is validated against measurements performed on this type of highly unconventional turbines.

The effectiveness of the gradient computation via the DA solver was instead examined by performing the fluid dynamic optimization of a 3D multirow turbine using almost 600 design variables. The optimization substantially improved the simulated turbine performance, while satisfying the imposed constraints. This also demonstrates the effectiveness and robustness of adjoint methods for multirow turbomachinery design problems in which a large number of design variables are involved.

It was furthermore found that the use of the CEV approximation in deriving the adjoint equations may lead to considerable inaccuracy of the computed gradient if the geometry to optimize operates at a low Mach number, whereas it is satisfactory in the case of transonic and supersonic blades.

Because of the general implementation of the RANS equations for arbitrary thermophysical models, this design framework can be applied, among others, to the automated design of 3D multistage turbomachinery operating in the nonideal flow regime like super-critical CO_2 compressors; high-speed compressors for refrigeration and air conditioning; oil and gas expanders and compressors; and turbomachinery for liquefied natural gas (LNG) systems and cryogenics. Future work will be therefore devoted to assess the gain in fluid dynamic performance attainable in these machines, for which best design practices are not well-established yet.

Acknowledgments

References

[1] Pierret, S., Filomeno Coelho, R., and Kato, H., "Multidisciplinary and Multiple Operating Points Shape Optimization of Three-Dimensional Compressor Blades," *Structural and Multidisciplinary Optimization*, Vol. 33, No. 1, 2007, pp. 61–70.
https://doi.org/10.1007/s00158-006-0033-y

[2] Lian, Y., and Liou, M.-S., "Multi-Objective Optimization of Transonic Compressor Blade Using Evolutionary Algorithm," *Journal of Propulsion and Power*, Vol. 21, No. 6, 2005, pp. 979–987.
https://doi.org/10.2514/1.14667

[3] Li, Z., and Zheng, X., "Review of Design Optimization Methods for Turbomachinery Aerodynamics," *Progress in Aerospace Sciences*, Vol. 93, Aug. 2017, pp. 1–23.
https://doi.org/10.1016/j.paerosci.2017.05.003

[4] Jameson, A., "Aerodynamic Design via Control Theory," *Journal of Scientific Computing*, Vol. 3, No. 3, 1988, pp. 233–260.
https://doi.org/10.1007/BF01061285

[5] Giles, M. B., and Pierce, N. A., "An Introduction to the Adjoint Approach to Design," *Flow, Turbulence and Combustion*, Vol. 65, No. 3, 2000, pp. 393–415.
https://doi.org/10.1023/A:1011430410075

[6] Kim, S., Alonso, J. J., and Jameson, A., "Multi-Element High-Lift Configuration Design Optimization Using Viscous Continuous Adjoint Method," *Journal of Aircraft*, Vol. 41, No. 5, 2004,

pp. 1082–1097.
https://doi.org/10.2514/1.17

[7] Nadarajah, S. K., and Jameson, A., "Optimum Shape Design for Unsteady Flows with Time-Accurate Continuous and Discrete Adjoint Method," *AIAA Journal*, Vol. 45, No. 7, 2007, pp. 1478–1491.
https://doi.org/10.2514/1.24332

[8] Nadarajah, S., and Jameson, A., "Optimum Shape Design for Unsteady Three-Dimensional Viscous Flows Using a Nonlinear Frequency-Domain Method," *Journal of Aircraft*, Vol. 44, No. 5, 2007, pp. 1513–1527.
https://doi.org/10.2514/1.27601

[9] Papadimitriou, D. I., and Giannakoglou, K. C., "Total Pressure Loss Minimization in Turbomachinery Cascades Using a New Continuous Adjoint Formulation," *Proceedings of the Institution of Mechanical Engineers, Part A: Journal of Power and Energy*, Vol. 221, No. 6, 2007, pp. 865–872.
https://doi.org/10.1243/09576509JPE463

[10] Corral, R., and Gisbert, F., "Profiled End Wall Design Using an Adjoint Navier–Stokes Solver," *Journal of Turbomachinery*, Vol. 130, No. 2, 2008, p. 8.
https://doi.org/10.1115/1.2751143

[11] Luo, J., Xiong, J., Liu, F., and McBean, I., "Three-Dimensional Aerodynamic Design Optimization of a Turbine Blade by Using an Adjoint Method," *Journal of Turbomachinery*, Vol. 133, No. 1, 2010, p. 11.
https://doi.org/10.1115/1.4001166

[12] Luo, J., Zhou, C., and Liu, F., "Multipoint Design Optimization of a Transonic Compressor Blade by Using an Adjoint Method," *Journal of Turbomachinery*, Vol. 136, No. 5, 2013, p. 10.
https://doi.org/10.1115/1.4025164

[13] Mousavi, A., and Nadarajah, S., "Adjoint-Based Multidisciplinary Design Optimization of Cooled Gas Turbine Blades," *49th AIAA Aerospace Sciences Meeting Including the New Horizons Forum and Aerospace Exposition*, AIAA Paper 2011-1131, 2011.
https://doi.org/10.2514/6.2011-1131

[14] Verstraete, T., Müller, L., and Müller, J.-D., "CAD-Based Adjoint Optimization of the Stresses in a Radial Turbine," *ASME Turbo Expo 2017: Turbomachinery Technical Conference and Exposition*, ASME, New York, 2017, p. 8.
https://doi.org/10.1115/GT2017-65005

[15] Wang, D. X., and He, L., "Adjoint Aerodynamic Design Optimization for Blades in Multistage Turbomachines—Part I: Methodology and Verification," *Journal of Turbomachinery*, Vol. 132, No. 2, 2010, p. 14.
https://doi.org/10.1115/1.3072498

[16] Wang, D. X., He, L., Li, Y. S., and Wells, R. G., "Adjoint Aerodynamic Design Optimization for Blades in Multistage Turbomachines—Part II: Validation and Application," *Journal of Turbomachinery*, Vol. 132, No. 2, 2010, p. 11.
https://doi.org/10.1115/1.3103928

[17] Walther, B., and Nadarajah, S., "Adjoint-Based Constrained Aerodynamic Shape Optimization for Multistage Turbomachines," *Journal of Propulsion and Power*, Vol. 31, No. 5, 2015, pp. 1298–1319.
https://doi.org/10.2514/1.B35433

[18] Walther, B., and Nadarajah, S., "Optimum Shape Design for Multirow Turbomachinery Configurations Using a Discrete Adjoint Approach and an Efficient Radial Basis Function Deformation Scheme for Complex Multiblock Grids," *Journal of Turbomachinery*, Vol. 137, No. 8, 2015, p. 20.
https://doi.org/10.1115/1.4029550

[19] Marta, A. C., and Shankaran, S., "On the Handling of Turbulence Equations in RANS Adjoint Solvers," *Computers & Fluids*, Vol. 74, March 2013, pp. 102–113.
https://doi.org/10.1016/j.compfluid.2013.01.012

[20] Economon, T. D., Palacios, F., Copeland, S. R., Lukaczyk, T. W., and Alonso, J. J., "SU2: An Open-Source Suite for Multiphysics Simulation and Design," *AIAA Journal*, Vol. 54, No. 3, 2015, pp. 828–846.
https://doi.org/10.2514/1.J053813

[21] Albring, T. A., Sagebaum, M., and Gauger, N. R., "Efficient Aerodynamic Design Using the Discrete Adjoint Method in SU2," *17th AIAA/ISSMO Multidisciplinary Analysis and Optimization Conference*, AIAA Paper 2016-3518, 2016.
https://doi.org/10.2514/6.2016-3518

[22] Sagebaum, M., Albring, T., and Gauger, N. R., "Expression Templates for Primal Value Taping in the Reverse Mode of Algorithmic Differentiation," *Optimization Methods and Software*, Vol. 33, Nos. 4–6, 2018, pp. 1207–1231.
https://doi.org/10.1080/10556788.2018.1471140

[23] Zhou, B. Y., Ryong Koh, S., Gauger, N. R., Meinke, M., and Schöder, W., "A Discrete Adjoint Framework for Trailing-Edge Noise Minimization via Porous Material," *Computers & Fluids*, Vol. 172,

Aug. 2018, pp. 97–108.
https://doi.org/10.1016/j.compfluid.2018.06.017

[24] Sanchez, R., Albring, T., Palacios, R., Gauger, N. R., Economon, T. D., and Alonso, J. J., "Coupled Adjoint-Based Sensitivities in Large-Displacement Fluid-Structure Interaction Using Algorithmic Differentiation," *International Journal for Numerical Methods in Engineering*, Vol. 113, No. 7, 2018, pp. 1081–1107.
https://doi.org/10.1002/nme.5700

[25] Vitale, S., Albring, T. A., Pini, M., Gauger, N. R., and Colonna, P., "Fully Turbulent Discrete Adjoint Solver for Non-Ideal Compressible Flow Applications," *Journal of the Global Power and Propulsion Society*, Vol. 1, Nov. 2017, pp. 252–270.
https://doi.org/10.22261/JGPPS.Z1FVOI

[26] Rubino, A., Pini, M., Colonna, P., Albring, T., Nimmagadda, S., Economon, T., and Alonso, J., "Adjoint-Based Fluid Dynamic Design Optimization in Quasi-Periodic Unsteady Flow Problems Using a Harmonic Balance Method," *Journal of Computational Physics*, Vol. 372, Nov. 2018, pp. 220–235.
https://doi.org/10.1016/j.jcp.2018.06.023

[27] Saxer, A. P., and Giles, M. B., "Quasi-Three-Dimensional Nonreflecting Boundary Conditions for Euler Equations Calculations," *Journal of Propulsion and Power*, Vol. 9, No. 2, 1993, pp. 263–271.
https://doi.org/10.2514/3.23618

[28] Stephan, B., Gallus, H. E., and Niehuis, R., "Experimental Investigations of Tip Clearance Flow and Its Influence on Secondary Flows in a 1-1/2 Stage Axial Turbine," *ASME Turbo Expo 2000: Power for Land, Sea, and Air*, ASME, New York, 2000, p. 12.
https://doi.org/10.1115/2000-GT-0613

[29] Yao, J., Davis, R. L., Alonso, J. J., and Jameson, A., "Massively Parallel Simulation of the Unsteady Flow in an Axial Turbine Stage," *Journal of Propulsion and Power*, Vol. 18, No. 2, 2002, pp. 465–471.
https://doi.org/10.2514/2.5957

[30] Jones, A. C., "Design and Test of a Small, High Pressure Ratio Radial Turbine," *ASME 1994 International Gas Turbine and Aeroengine Congress and Exposition*, ASME, New York, 1994, p. 12.
https://doi.org/10.1115/94-GT-135

[31] Keep, J. A., Vitale, S., Pini, M., and Burigana, M., "Preliminary Verification of the Open-Source CFD Solver SU2 for Radial-Inflow Turbine Applications," *Energy Procedia*, Vol. 129, Sept. 2017, pp. 1071–1077.
https://doi.org/10.1016/j.egypro.2017.09.130

[32] Denton, J. D., "Loss Mechanisms in Turbomachines," *ASME 1990 International Gas Turbine and Aeroengine Congress and Exposition*, ASME, New York, 1993, p. 40.
https://doi.org/10.1115/93-GT-435

[33] Saxer, A. P., and Giles, M. B., "Predictions of Three-Dimensional Steady and Unsteady Inviscid Transonic Stator/Rotor Interaction with Inlet Radial Temperature Nonuniformity," *Journal of Turbomachinery*, Vol. 116, No. 3, 1994, pp. 347–357.
https://doi.org/10.1115/1.2929421

[34] Palacios, F., Alonso, J., Duraisamy, K., Colonno, M., Hicken, J., Aranake, A., Campos, A., Copeland, S., Economon, T., Lonkar, A., et al., "Stanford University Unstructured (SU2): An Open-Source Integrated Computational Environment for Multi-Physics Simulation and Design," *51st AIAA Aerospace Sciences Meeting Including the New Horizons Forum and Aerospace Exposition*, AIAA Paper 2013-287, 2013.
https://doi.org/10.2514/6.2013-287

[35] Dwight, R. P., "Robust Mesh Deformation Using the Linear Elasticity Equations," *Computational Fluid Dynamics 2006*, edited by H. Deconinck, and E. Dick, Springer, Berlin, 2009, pp. 401–406.
https://doi.org/10.1007/978-3-540-92779-2_62

[36] Sederberg, T. W., and Parry, S. R., "Free-Form Deformation of Solid Geometric Models," *ACM SIGGRAPH Computer Graphics*, Vol. 20, No. 4, 1986, pp. 151–160.
https://doi.org/10.1145/15922.15903

[37] Bahamonde, S., Pini, M., De Servi, C., Rubino, A., and Colonna, P., "Method for the Preliminary Fluid Dynamic Design of High-Temperature Mini-Organic Rankine Cycle Turbines," *Journal of Engineering for Gas Turbines and Power*, Vol. 139, No. 8, 2017, p. 14.
https://doi.org/10.1115/1.4035841

[38] *AutoGrid5: Automated Grid Generator for Turbomachinery*, NUMECA International, Brussels, 2010, https://www.numeca.com/product/autogrid5.

[39] Menter, F., "Zonal Two Equation k–ω Turbulence Models for Aerodynamic Flows," *23rd Fluid Dynamics, Plasmadynamics, and Lasers Conference*, AIAA Paper 1993-2906, 1993.
https://doi.org/10.2514/6.1993-2906

[40] Roe, P. L., "Approximate Riemann Solvers, Parameter Vectors, and Difference Schemes," *Journal of Computational Physics*, Vol. 135, No. 2, 1997, pp. 250–258.
https://doi.org/10.1006/jcph.1997.5705

[41] Blazek, J., *Computational Fluid Dynamics: Principles and Applications*, Butterworth–Heinemann, Oxford, 2005.
https://doi.org/10.1016/C2013-0-19038-1

[42] Yao, J., Jameson, A., Alonso, J. J., and Liu, F., "Development and Validation of a Massively Parallel Flow Solver for Turbomachinery Flows," *Journal of Propulsion and Power*, Vol. 17, No. 3, 2001, pp. 659–668.
https://doi.org/10.2514/2.5793

[43] Sauret, E., "Open Design of High Pressure Ratio Radial-Inflow Turbine for Academic Validation," *ASME 2012 International Mechanical Engineering Congress and Exposition*, ASME, New York, 2012, pp. 3183–3197.
https://doi.org/10.1115/IMECE2012-88315

[44] Verstraete, T., "CADO: A Computer Aided Design and Optimization Tool for Turbomachinery Applications," *2nd International Conference on Engineering Optimization*, Lisbon, Portugal, Sept. 2010, pp. 6–9.

[45] Van Albada, G., Van Leer, B., and Roberts, W., "A Comparative Study of Computational Methods in Cosmic Gas Dynamics," *Upwind and High-Resolution Schemes*, edited by M. Yousuff Hussaini, B. van Leer, and J. Van Rosendale, Springer, Berlin, 1997, pp. 95–103.
https://doi.org/10.1007/978-3-642-60543-7_6

[46] Rubechini, F., Marconcini, M., Giovannini, M., Bellucci, J., and Arnone, A., "Accounting for Unsteady Interaction in Transonic Stages," *Journal of Engineering for Gas Turbines and Power*, Vol. 137, No. 5, 2015, p. 9.
https://doi.org/10.1115/1.4028667

[47] Montagne, J. L., and Vinokur, J. L., "Generalized Flux-Vector Splitting and Roe Average for an Equilibrium Real Gas," *Journal of Computational Physics*, Vol. 89, No. 2, 1990, pp. 276–300.

[48] Vitale, S., Gori, G., Pini, M., Guardone, A., Economon, T. D., Palacios, F., Alonso, J. J., and Colonna, P., "Extension of the SU2 Open Source CFD Code to the Simulation of Turbulent Flows of Fluids Modelled with Complex Thermophysical Laws," *22nd AIAA Computational Fluid Dynamics Conference*, AIAA Paper 2015-2760, 2015.
https://doi.org/10.2514/6.2015-2760

[49] Kraft, D., "A Software Package for Sequential Quadratic Programming," DLR German Aerospace Center–Inst. for Flight Mechanics Dfvlr-fb 88-28, Oberpfaffenhofen, 1988.

[50] Spalart, P., and Allmaras, S., "A One-Equation Turbulence Model for Aerodynamic Flows," *30th Aerospace Sciences Meeting and Exhibit*, AIAA Paper 1992-439, 1992.
https://doi.org/10.2514/6.1992-439

[51] Mueller, L., and Verstraete, T., "CAD Integrated Multipoint Adjoint-Based Optimization of a Turbocharger Radial Turbine," *International Journal of Turbomachinery, Propulsion and Power*, Vol. 2, No. 3, 2017, p. 14.
https://doi.org/10.3390/ijtpp2030014

J. P. Bons
Associate Editor